EXPLORING POTENTIAL MECHANISMS RESPONSIBLE FOR OBSERVED CHANGES OF ULTRASONIC BACKSCATTERED ENERGY WITH TEMPERATURE VARIATIONS

BY

XIN LI

THESIS

Submitted in partial fulfillment of the requirements
for the degree of Master of Science in Nuclear, Plasma, and Radiological Engineering
in the Graduate College of the
University of Illinois at Urbana-Champaign, 2013

Urbana, Illinois

Master's Committee:

Associate Professor Michael L. Oelze, Chair
Associate Professor Ling Jian Meng

ABSTRACT

Hyperthermia has been proven to be an effective way of enhancing radiotherapy and chemotherapy, but monitoring the temperature accurately and noninvasively is imperative for controlling the exposures. Ultrasound thermometry techniques have been proposed, such as tracking echo shifts or correlating the changes in backscattered energy (CBE) with temperature. Previous studies have provided the observation that the ultrasonic backscattered energy from a tissue region will change due to a change of temperature. The mechanism responsible for the CBE with temperature has been hypothesized to be from the changes in scattering properties of local aqueous and lipid scatterers. A new mechanism is hypothesized to be responsible for much of the observed CBE versus temperature rise, i.e., changes in signal coherence. To test this hypothesis, simulations were conducted in software phantoms and the CBE was calculated versus changes in SOS, which are typically associated with changes in temperature. The simulations were carried out with a linear array having 128 elements and center frequency of 5.5 MHz. Experiments were carried out by scanning physical phantoms containing randomly spaced glass beads with a Sonix RP scanner at every 0.5 ºC from 37 ºC to 48 ºC. Shifts in the backscattered signal caused by changes of SOS with temperature were compensated using 2D motion compensation techniques. Each pixel in the CBE image underwent either a monotonic increase (up to 7.1 dB) or a monotonic decrease (down to -4.6 dB) with increasing temperature. Similar CBE curves were also produced at a fixed temperature by shifting the elevation image plane location or by

shifting the focus of the linear array probe. Therefore, using CBE curves to monitor temperature elevation may not be robust against tissue motion. Furthermore, the production of CBE curves versus temperature did not require the presence of lipid and aqueous scatterers.

ACKNOWLEDGEMENTS

First, I would like to acknowledge my research advisor Dr. Michael Oelze for his ideas and support on this project. I would express my gratitude to the help of Goutam Ghoshal for his help on setting up of experiment hard wares and making experiment phantoms. Professor Roberto J. Lavarello shall be recognized for helping on the simulation part and suggestions for improving the experiment. Finally, I wish to acknowledge the technical assistance of Jeremy Kemmerer, Adam Luchies, and Billy Ridgway. The work was supported by NIH Grant R01 EB008992 (National Institutes of Health, Bethesda, MD).

TABLE OF CONTENTS

CHAPTER 1 INTRODUCTION

1.1 Background

Hyperthermia in the range of 40 ºC to 44 ºC has been used in cancer treatment to synergistically enhance chemotherapy and radiotherapy [1-4]. In fact, hyperthermia is one of the best known and most potent radiosensitizers to date [5] [6]. In the 1970s, ultrasound was investigated as a means to elevate and maintain tissue temperature around 43ºC. However, this technology requires accurate non-invasive monitoring of the temperature of heated tissue. Therefore, non-invasive mapping of temperature is imperative for monitoring ultrasound-based hyperthermia and ablative therapy techniques [7].

1.2 Motivation

Various imaging modalities have been examined for their ability to monitor temperature, such as computed tomography (CT), magnetic resonance imaging (MRI), electrical impedance tomography (EIT), and ultrasound thermometry. Although CT can provide the sensitivity and spatial resolution needed to map temperature (fraction of ºC at 1 cm resolution) [8], the radiation exposure from repeated CT measurements needs to stay in reasonable range, which makes it not ideal for real-time monitoring of temperature for hyperthermia or ablative treatment [9]. MRI can achieve the needed sensitivity and spatial resolution, (less than 1 cm spatial resolution and 1ºC sensitivity [10]) without creating radiation dose, but it has other limitations such as high cost

and incompatibility with certain devices used for heating [11]. The EIT method suffers from nonlinearity issues and is an ill-posed reconstruction problem; therefore, achieving sufficient spatial resolution is difficult [8]. Hence, a need exists to develop imaging techniques with adequate spatial and temporal resolution, with real-time or near real-time feedback and with robustness against tissue motion to monitor temperature during therapy.

Among acoustic thermometry, there exist several methods for estimating temperature from backscattered signals. To date, most work in acoustic thermometry has centered on estimating the temperature through estimation of the temperature-dependent speed of sound (SOS) in tissue [13-16]. The most common technique for estimating SOS is to estimate the temperature-dependent echo shifts due to changes in both SOS and tissue expansion [17-20]. The echo shift method can provide accurate estimates of the local temperature, but the technique requires prior knowledge of the thermal expansion coefficient and the SOS dependence on temperature for a specific tissue [18]. The method of estimating temperature based on attenuation coefficient has been studied [21-24], but one major problem is that the attenuation coefficient will change appreciably only up to 50 ºC, which makes it not ideal for hyperthermia. Furthermore, the attenuation is highly dependent on tissue state and changes when tissues undergo irreversible changes due to thermal therapy.

1.3 Literature review on the change of backscattered energy theory

Another method based on ultrasonic signals that has been proposed for thermometry is to correlate temperature elevations with changes in the backscattered energy (CBE) [25-28]. The CBE method has been examined for its ability to monitor tissue temperature. Previous studies in *ex vivo* samples of liver and turkey breast have demonstrated that the changes in the CBE can be correlated with changes in the temperature of the tissue sample [28]. Similar to the echo shift methods, this method needs tissue specific calibration [26] and requires registration from one frame to the next. The CBE has been hypothesized to be produced by changes in the local scattering from lipid and aqueous scatterers in the tissues versus temperature. According to the hypothesis, the temperature changes would produce a decrease in the CBE for regions dominated by aqueous scatterers and an increase in the CBE for regions dominated by lipid scatterers [28].

While this mechanism may help elucidate the CBE observed in tissues due to temperature elevations, other mechanisms may also contribute significantly to the CBE. In this study, it is hypothesized that the CBE could also be attributable to local changes in coherent summation of ultrasonic pulses scattered from sub-resolution scatterers and not necessarily changes in the scattering cross section of the underlying scatterers. The changes in the coherent summation of the scattered wavelets would be due to multiple factors such as changes in

SOS with temperature, attenuation coefficient changes, scatter position changes, drifting of scanning plane and drifting of focus during scanning.

1.4 Organization

Chapter II of this thesis introduces the basic theory and data processing methods in estimating CBE. Chapter III contains simulations for predicting the CBE by solely changing the SOS and not from lipid and aqueous scatterers. Physical experiments were then conducted to calculate the CBE from physical phantoms by elevating water bath temperature, by changing the elevational scanning plane or by changing the axial position of the acoustic transducer array. Chapter IV provides the results from the simulation and experiments. Chapter V discusses the results and provides a hypothesis of alternate mechanisms of production of CBE curves.

CHAPTER 2 THEORY

2.1 Introduction

Conventional ultrasonic imaging techniques use the backscattered signal to construct images. A B-mode image is formed by aligning the envelope detected scan lines from the transducer array. The reflection signal from one scan line is illustrated in Fig. 1. By choosing appropriate time delays, the signal can be focused on transmit at one location and on receive the signal can be focused at all depths by using dynamic time delays.

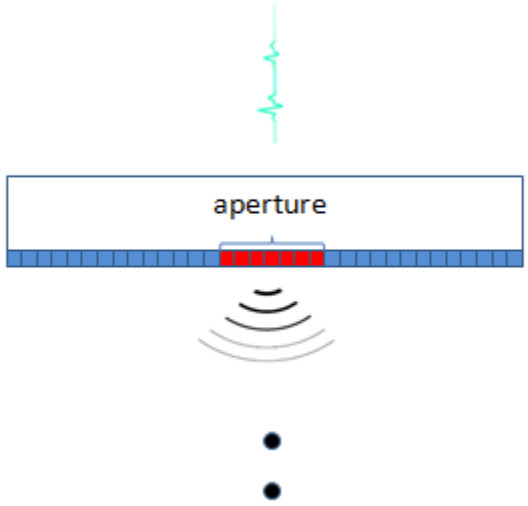

Figure 1. The illustration of how a scan line signal is acquired. The red elements form the transmit and receive sub-aperture. .

From Fig. 1, it can be observed that the reflection signal at one single scan line is acquired by summation of the reflection signal from the two scatterers. The coherent summation of signals from sub-resolution scatterers forms the “speckle pattern”. The speckle pattern depends on different factors, such as

the scattered pulse length and pulse shape, the center frequency of the pulse, the beam width of the imaging system, and the density and spatial organization of the scatterers. By changing the interference pattern, destructive interference (i.e., a local decrease in the signal amplitude) or constructive interference (i.e, an increase in the local signal amplitude) can occur. An example of the destructive and constructive interference caused by two scatterers with slightly offset positions is illustrated in Fig. 2. The two pulses sum together with only slightly different time offsets resulting in destructive or constructive interference. From the two summed signals in Fig .2, the CBE was observed increase by 6 dB from the destructive to constructive case.

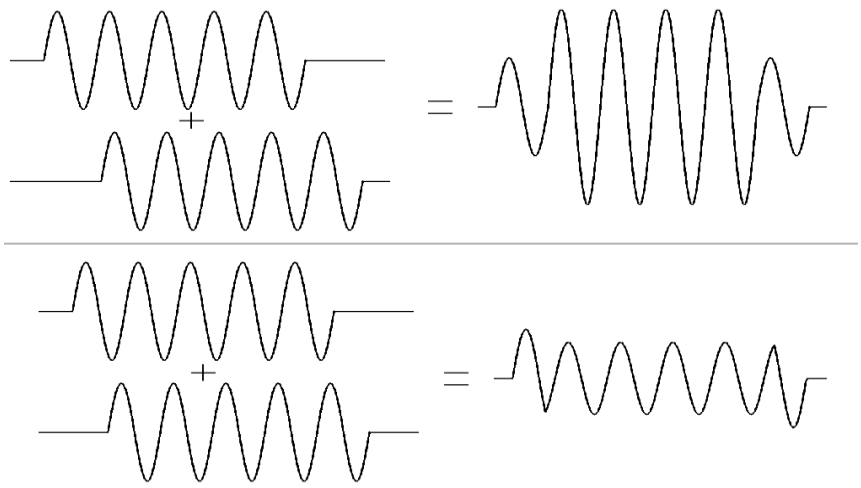

Figure 2. Depiction of constructive interference from two summed pulses (top) and depiction of destructive interference from two summed pulses (bottom) after a slight shift in their arrival time.

The change of SOS can induce small time offsets resulting in a different speckle pattern. Aside from changes in SOS leading to CBE, shifting of the focus due to axial motion and the elevational drifting of the scanning plane due to elevational motion could also affect the image speckle pattern and subsequent CBE estimate. An independent speckle profile can be obtained if a new frame is acquired that is at least a beamwidth apart in the elevational direction. In acquiring sequential image frames from a subject, slight motion can occur in the elevational plane (less than a beamwidth) due to tissue motion or probe motion. As a result, consecutive frames may yield only partially correlated speckle patterns. Because the speckle pattern changes, the subsequent CBE may also mimic the effects observed due to temperature changes. Similar to elevational displacement, it is possible that when capturing sequential image frames that motion can cause the probe to shift to a different axial location, causing the relative motion between the focus and the region of interest. This effect will also influence the calculated CBE because a new speckle pattern can be generated.

2.2 Shifting compensation method

In hyperthermia, because the temperature of tissue is raised, the SOS in the tissue will also change. For example, the SOS in water at 30ºC is 1507 m/s, whereas the SOS in water at 50ºC is 1541 m/s. If the tissue temperature rises, the SOS will increase, thus creating an apparent shrinkage in the axial

dimension in the B-mode image. For example, if two surfaces are 1cm apart from each other at 30ºC in water, they will appear 531 pixels apart (~13.3 us) under a sampling rate of 40 MHz. However, at 50ºC, they will appear 519 pixels apart (~13.0 us).

Aside from the apparent shifts caused by the change of SOS, probe motion might also occur during scanning, such as motion caused by thermal expansion, slight deforming of supporting materials, respiration, etc. Currently, motion estimation is an important research area in ultrasound imaging [29-33]. These methods are based on speckle tracking in two dimensions. Much of this research has been adopted to guide high intensity focused ultrasound (HIFU), rather than accurately estimating the temperature map around the focus of a HIFU source [34-37].

A. Rigid motion compensation

To compensate for the apparent tissue motion from temperature elevations, rigid and non-rigid registration technique can be utilized. The rigid motion compensation method compensates “rigid” tissue motion within the imaging plane. Rigid motion assumes all of the elements within a block shift with the same magnitude, whereas non-rigid motion allows for spatially-dependent motion within the block where the shifts are not necessarily the same for each element within the block.

To map the temperature, it is required to estimate the shifts associated with the changes in SOS. The method used to estimate the shifts is similar to a 2D cross-correlation method. Specifically, a frame is chosen at a reference temperature and a small region is used to track and analyze in subsequent frames, as demonstrated in Fig. 3.

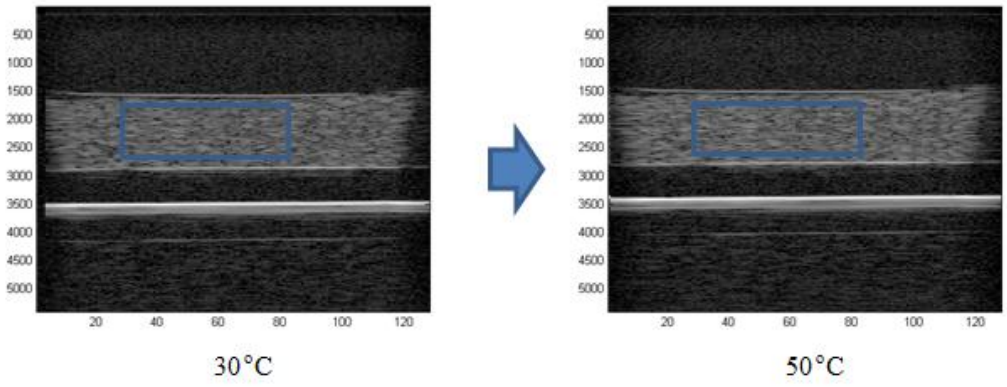

Figure 3. Illustration of direct registration with the reference frame at 30 ℃.

In the temperature experiments at every 0.5 ºC, a B-mode image is captured. Use Fig. 3 as an example of the temperature experiments. After capturing a frame, the region inside the blue block is tracked in the subsequent frames through 2D cross-correlation, within a small vicinity of the position of the original blue block in the reference image. The block was chosen to have an axial length of 20 μm and a lateral length of 300 um. However, when the temperature change is large, the changes in the speckle pattern are too large, so that even the 2D cross-correlation technique will produce a large error.

In practical application, each consecutive frame is registered to the previous frame, rather than the original frame. For example, the frame at 30 ºC is used as a reference to track the position of data block at 30.5 ºC, then the frame at 30.5 ºC is used as a reference to track the position of data block at 31 ºC (see Fig. 4).

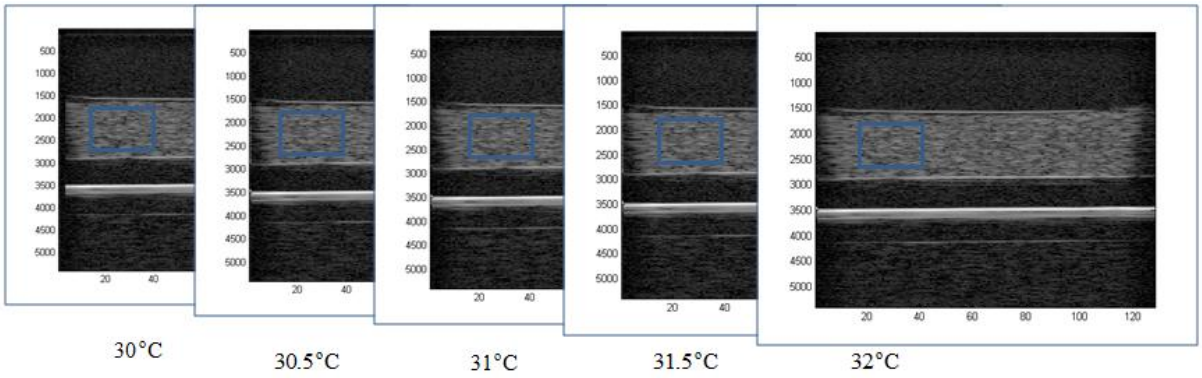

Figure 4. Illustration of serial registration, where each previously acquired frame is used to track the position of the data block of current frame.

The motion vector is calculated as:

$$(a,b)=\arg\max_{a,b}\{\sum_{m,n} img_{ref}(m,n)\times img_{new}(m+a,n+b)\}. \qquad (2.1)$$

Where img_{ref} refers to the reference frame, and img_{new} stands for the current frame to be analyzed. Unfortunately, the 2D cross-correlation method cannot be applied directly even under serial registration. If the vector is found using the equation above, the error will be large. A modified version improves the

error of the registration and is given by,

$$(a,b)=\arg\max_{a,b}\{\frac{\sum_{m,n} img_{ref}(m,n)\times img_{new}(m+a,n+b)}{\sqrt{\sum_{m,n} img^{2}{}_{new}(m+a,n+b)}}\}. \quad (2.2)$$

The purpose of the extra term is to penalize regions with very high signal magnitude, because high signal magnitude regions can dominate the summation, which can cause the tracked region to deviate from the correct region to the region with high signal magnitude.

B. Non-rigid motion compensation

The non-rigid motion compensation will not only compensate for rigid motion caused by tissue-probe motion, but also compensate for non-rigid motion such as the “shrinkage” caused by the rise of temperature and deformation of tissue due to temperature change. A very small block of axial length of 9 pixels and lateral length of 3 pixels around the pixel being registered is used to track each pixel’s position. Instead of tracking a large region of data all together with a large data block, the non-rigid method will track each pixel’s position separately giving a more precise result at a cost of a higher computation. Each pixel has a separate motion vector given by,

$$(a,b)_{i,j} = \arg\max_{a,b}\{\frac{\sum_{m,n} img_{ref}(m,n) \times img_{new}(m+a,n+b)}{\sqrt{\sum_{m,n} img^{2}{}_{new}(m+a,n+b)}}\} \quad (2.3)$$

where (m,n) are the index of pixels within the tracking block, whose size is only 9 pixels in the axial direction and 3 pixels in lateral direction. At each temperature, the motion vector of each pixel is updated.

2.3 Calculation of CBE

The CBE was calculated from the registered frames by comparing the intensity of images at a particular temperature with the reference image at 37 ºC. Before making the frame to frame comparisons, it was first necessary to register the images to account for apparent motion using the methods outlined above. A box of axial length of 13.3 mm and lateral length of 28.2 mm was used to track a large region of the phantom (Fig. 5). Both of the tracking methods (i.e., rigid and non-rigid) were used to search in the vicinity of original image block by 20 µm in axial direction and 300 µm in lateral direction to register the image.

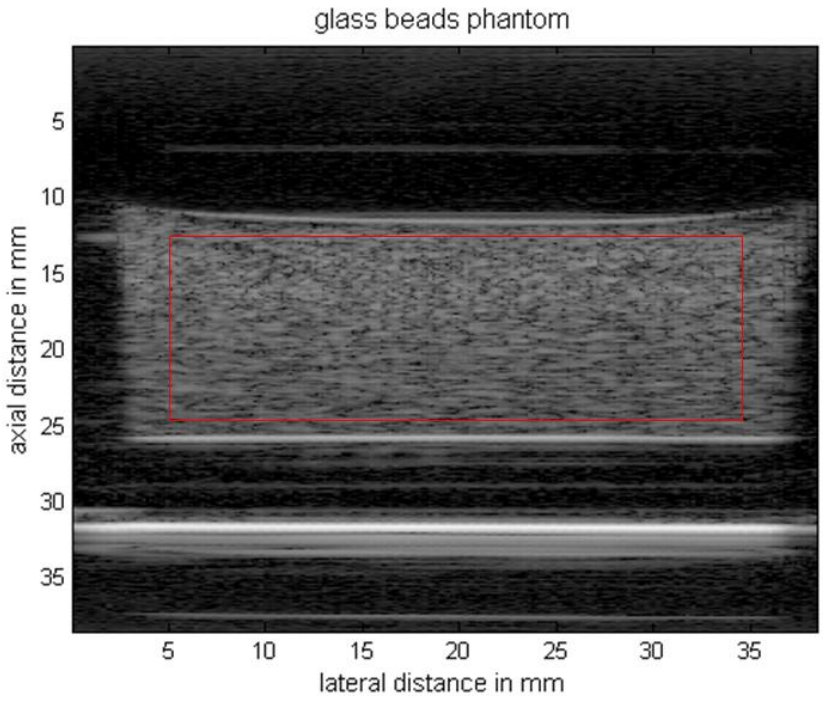

Figure 5. B-mode image of the glass bead phantom. Data were chosen within the larger data block (red boundary), and then continued to be tracked in each frame using a 2D motion compensation method.

After registration, the envelope values were squared to determine the backscattered energy at each pixel in the image. The pixel's axial length was about 18.5 um and lateral length was 0.297 mm. The CBE was estimated by comparing the backscattered energy at each pixel in the ROI at a particular temperature with that of the reference temperature (37 ºC). The CBE in dB was calculated as,

$$CBE_T(i,j) = 10\log_{10}\frac{env_T{}^2(i,j)}{env_{37^oC}{}^2(i,j)} \qquad (2.4)$$

Where the $env_T(i,j)$ stands for the pixel value of the envelope at coordinate (i,j) and temperature *T*. The CBE values were then mapped

into a CBE image. The positive and negative CBE curves were calculated by averaging the values of all the positive pixels in the CBE image together and that of all the negative pixels together at each step (i.e., change in temperature, SOS, elevational displacement or axial displacement). The positive and negative CBE values are given by,

$$\begin{aligned} CBE_{positive}(T) &= mean(\{CBE_T(i,j) > 0\}) \\ CBE_{\text{negative}}(T) &= mean(\{CBE_T(i,j) < 0\}) \end{aligned}. \qquad (2.5)$$

CHAPTER 3 SIMULATIONS AND EXPERIMENT METHODS

3.1 Introduction

Simulations were conducted to test the effect of SOS changes on CBE. These simulations were carried out to predict the amount of CBE that results from simple SOS changes and without changes in the scattering cross sections of sub-resolution scatterers. Temperature experiments was also carried out with agar-glass bead phantoms to test the hypothesis that change of SOS can solely lead to CBE positive and negative deviation. In addition to these experiments, elevational and axial displacement effects were also tested with the physical phantoms.

3.2 Simulations of CBE with change of SOS

Simulations were carried out to test the hypothesis that solely changing the SOS can give rise to CBE curves. Backscattered data from a simulated phantom of lateral length 4 cm, elevational length 0.5 cm and axial length 1.5 cm was simulated using FIELD II [38] [39]. The SOS of the background was increased from 1520 m/s to 1540 m/s at 2 m/s increments (which corresponds to a typical SOS change induced by raising the temperature from 37 ºC to 48 ºC in water [40]). The reflectivity of the individual scatterer was programmed not to change as a function of SOS or temperature. The backscattered signal simulated to come from an array. The simulated array had 128 elements (3.8 cm width), center

frequency of 5.5 MHz, and transmitting and receiving aperture of 32 elements in the first simulation (a second simulation used 64 elements on transmit). At each SOS, a B-mode image was constructed by the transducer with the focusing delays calculated from focusing at the 2.7cm depth (center of phantom in depth) with SOS of 1520 m/s (SOS of reference image). CBE images were created after correcting for apparent displacements using both rigid and non-rigid motion compensation.

The two simulations were carried out using different f-numbers. The f-number of a source is the ratio of the focal distance to the aperture diameter or size. By decreasing the f-number, the focal depth and beamwidth would be smaller and effects of coherence changes would be more enhanced versus changes in SOS. The f-number was changed by modifying the transmission aperture size from 32 to 64 elements while maintaining the same focal distance.

3.3 Temperature Experiment

A clinical ultrasound imaging system (Sonix RP, Ultrasonix Inc, Canada) was used to scan agar phantoms with uniformly distributed glass beads. A linear array with 128 elements (L14-5/38, Ultrasonix Inc, Canada) with a center frequency measured at 5.5 MHz was used in experiments. Figure 6 shows a diagram of the experimental setup used in the experiments. Scans were

conducted with the Sonix RP system and radio frequency (RF) data were stored for post-processing. RF data were acquired at a 40 MHz sampling rate. In the first experiments, transmission aperture and reception aperture size were both set to 32 elements. The focus was placed at the depth of 2.7 cm (center of phantom in depth and the same as the simulated source) at the reference temperature 37 ºC. The time delay of each element was the same for each temperature (the dynamic focusing on reception was disabled). Another transmission aperture size of 64 elements was also used in order to decrease the f-number and test the effects of a different transmission f-number on CBE.

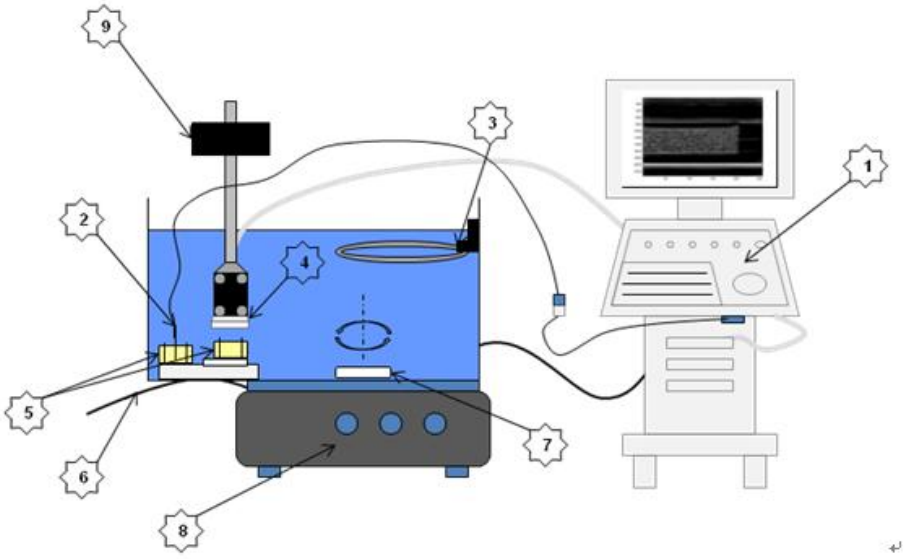

Figure 6. Configuration of experiment setup: 1. Sonix RP imaging system. 2. Thermocouple. 3. Electric heater. 4. Linear array probe. 5. Phantom used to measure the temperature and phantom being scanned. 6. RS232 serial port cable for communication between the Daedal positioning system and the Sonix RP imager. 7. Magnetic stir bar. 8. Magnetic stirrer. 9. Arm of Daedal positioning system.

The Physical phantoms were constructed for the experiments. They were made with 100 ml of degassed water, 2.5 g of agar and 1.0 g of glass beads (45-53 μm in diameter). Six phantoms were made as small cylinders with dimensions of 3.0 cm diameter and 1.5 cm thickness. Figure 7 is an illustration of one of the phantoms.

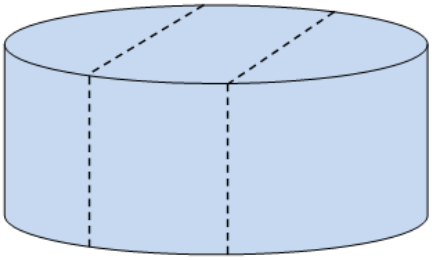

Figure 7. Illustration of the cylindrical phantoms in the experiments. A cut along the dotted line was made to make the phantom thinner, thus allowing more homogeneous temperature profile inside the phantom.

Degassed water was added to a water tank along with a heating coil (SF30, Waage Electric, Inc, Kenilworth, NJ, USA) to adjust the temperature of the water. A magnetic stir bar was used in order to heat the water more uniformly in the tank. A phantom was placed carefully on a marked position in the water tank and was pinned to the Plexiglas plate in the water tank to prevent it from moving while the water was stirred (Fig. 6). A thermocouple was inserted into

another phantom outside of the scan region in order to monitor the temperature in the phantom but avoid imaging the thermocouple

The Sonix RP was programmed with C++ and LabVIEW to work with the thermocouple to capture frames automatically at every 0.5 ºC from 37 ºC to 48 ºC. When the temperature reached 50 ºC, the heating was stopped.

At each temperature, the CBE was calculated from within a data block (axial length 13.3 mm, lateral length 28.2 mm) selected from the B-mode images (Fig. 5). Following the procedure outlined above, the CBE image and CBE curves were calculated.

3.4 Elevational displacement experiment

Elevational displacements will also change the speckle pattern providing a new realization of the coherence pattern. The shifting coherence is hypothesized to result in CBE curves. To test the hypothesis that displacements in the elevational direction (that may be caused either by tissue or probe motion) can provide CBE curves similar to the ones obtained from temperature experiment, agar phantoms were scanned by moving the probe in the elevational direction with a step size of 10 um. The -3 dB elevational beamwidth at the elevational focusing depth of 1.6 cm was calculated to be 1.1 mm, (i.e., the L14-5/38 probe has an elevational focus at depth of 1.6 cm). The Sonix RP system was

programmed to communicate with a high resolution positioning system (Daedal positioning system, Daedal Inc, Harrison, PA, USA) via a RS232 serial port. Image frames were captured after moving the transducer probe in the elevational direction step by step from 0 μm to 500 μm. The CBE was then calculated for the same region in the images. Because there is no motion in the imaging plane, no motion compensation was needed.

3.5 Axial displacement experiment

Axial displacements can also change the local coherence because the focus can shift providing a different speckle pattern due to shifting local beam properties. This in turn is hypothesized to produce CBE curves. An experiment was conducted to shift the axial distance between the probe and the phantom without changing temperature or elevational displacement. The initial focus was set at depth of 1.8 cm. The image frames were captured while moving the probe up by 750 μm at the step size of 10 μm. Therefore, the corresponding focus was moved from a depth of 1.8 cm to 1.725 cm in 75 steps corresponding to a step size of 10 μm. The motion was compensated simply by shifting the region of interest (the block of data used in the CBE estimates) up by 10 um for every frame. The CBE image and CBE curve were calculated using the same methodology as the simulation and temperature experiments.

CHAPTER 4 RESULTS

4.1 Results for simulation

The CBE images resulting from the simulations are shown in Fig. 8, with both 32 and 64 elements on transmission and processing the data with both rigid and non-rigid 2D cross-correlation motion tracking. The corresponding CBE curves are shown in Fig. 9. The CBE curves were observed to monotonically increase or decrease versus SOS. These changes are similar to the results observed in [28]. However, the CBE curves in the simulations were not attributable to local changes in scattering properties of lipid and aqueous scatterers because the only changing parameter was the SOS, i.e., the scattering cross section was set not to change at all in the simulations.

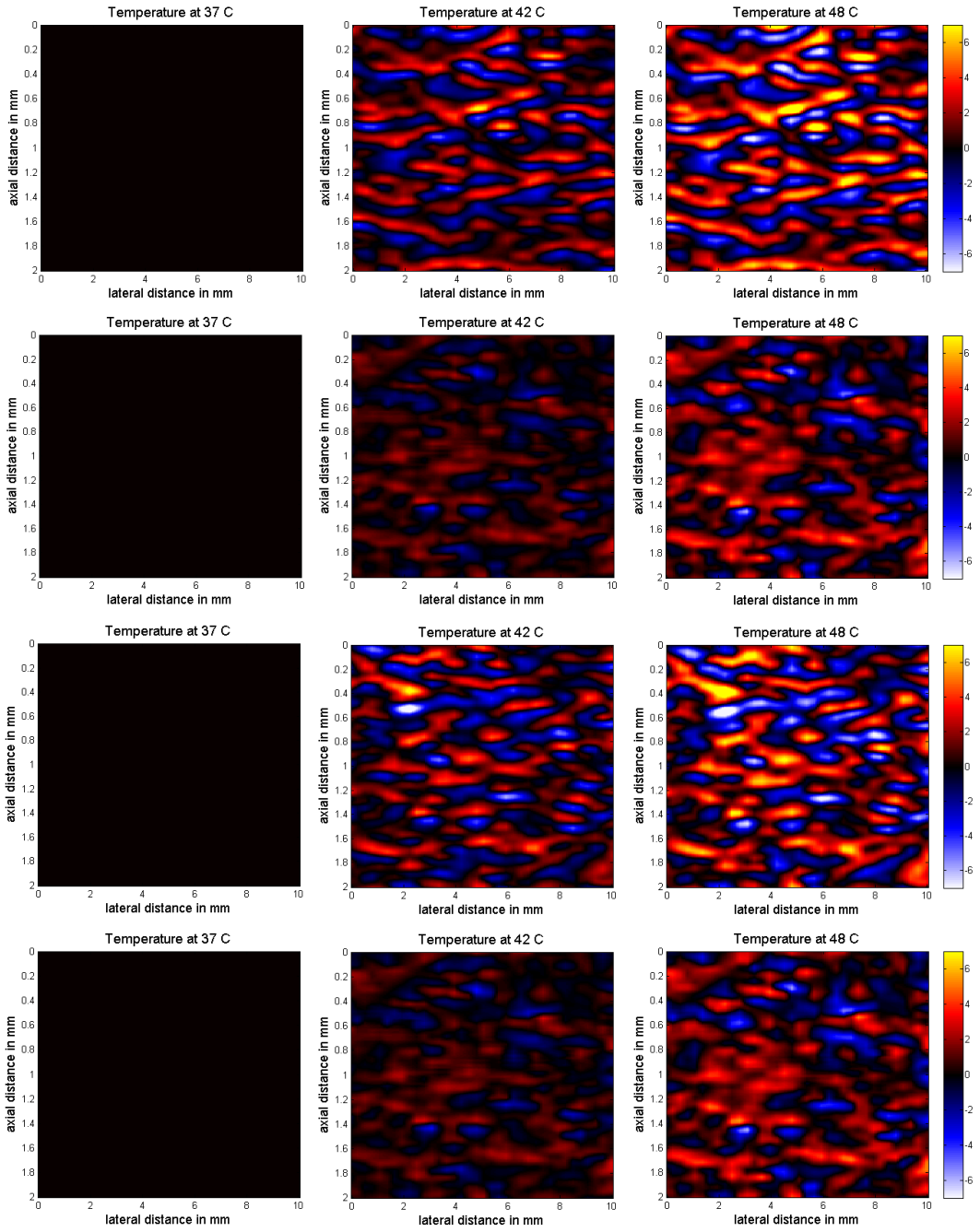

Figure 8. CBE images of simulation: First row: Transmitting and receiving with 32 elements with rigid motion tracking method; Second row: Transmitting and receiving with 32 elements with non-rigid motion tracking method; Third row: Transmitting with 64 elements, receiving with 32 elements with rigid motion tracking method; Fourth row: Transmitting with 64 elements, receiving with 32 elements with non-rigid motion tracking method.

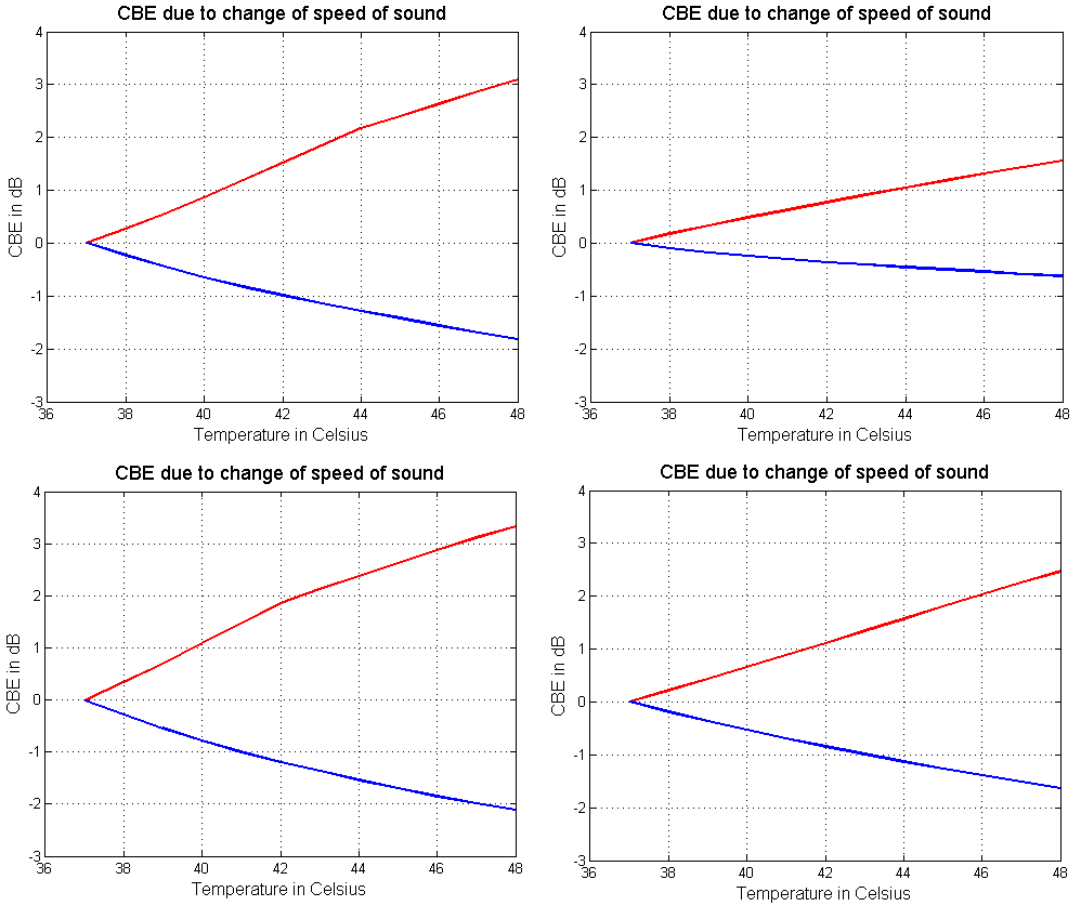

Figure 9. CBE curves of simulation: Upper left: Transmitting and receiving with 32 elements with rigid motion tracking method; Upper right: Transmitting and receiving with 32 elements with non-rigid motion tracking method; Lower left: Transmitting with 64 elements, receiving with 32 elements with rigid motion tracking method; Lower right: Transmitting with 64 elements, receiving with 32 elements with non-rigid motion tracking method. The red line is the positive CBE curve, the blue line is the negative CBE curve.

From Fig. 8, the CBE image is observed; however, as mentioned above, the scatterer's property was set not to change. The only changing parameter is the speed of sound from 1520 m/s to 1540 m/s. From Fig. 9, the CBE curve is formed, the result is similar as Fig. 17 with both positive and negative deviation

curves. From both Figs. 8&9, the impacts caused by the different transmitting aperture and different data processing methods can be seen. The larger the transmitting aperture is (64 instead of 32 elements, which correspond to a smaller f-number), the larger CBE will be achieved (a brighter CBE image in Fig. 8 and a larger CBE curve deviation in Fig 9). And the non-rigid motion tracking method yields lower CBE than the rigid motion tracking method.

4.2 Results for temperature experiment

CBE images from the physical phantom are shown in Fig. 10 for 37 ºC, 42 °C and 48 °C, with both 32 and 64 elements on transmission and processing the data with both rigid and non-rigid motion tracking methods. From Fig. 10, it can be observed in some regions that the CBE was positive while in other regions the CBE was negative. The resulting CBE curves versus temperature were plotted in Fig. 11. Again, different results were achieved with different transmitting f-numbers and different motion tracking methods. From Fig. 11, the familiar shapes of the positive and negative CBE curves versus temperature are present, which agrees with observations made in [25-28], in which both positive (up to around 5 dB) and negative curve (down to around -3 dB) is approximately linear with the increase of temperature. Still since there is no lipid and aqueous scatterers in our phantom, the results indicate that some other effects could also caused such CBE effects, such as a change of SOS due to temperature.

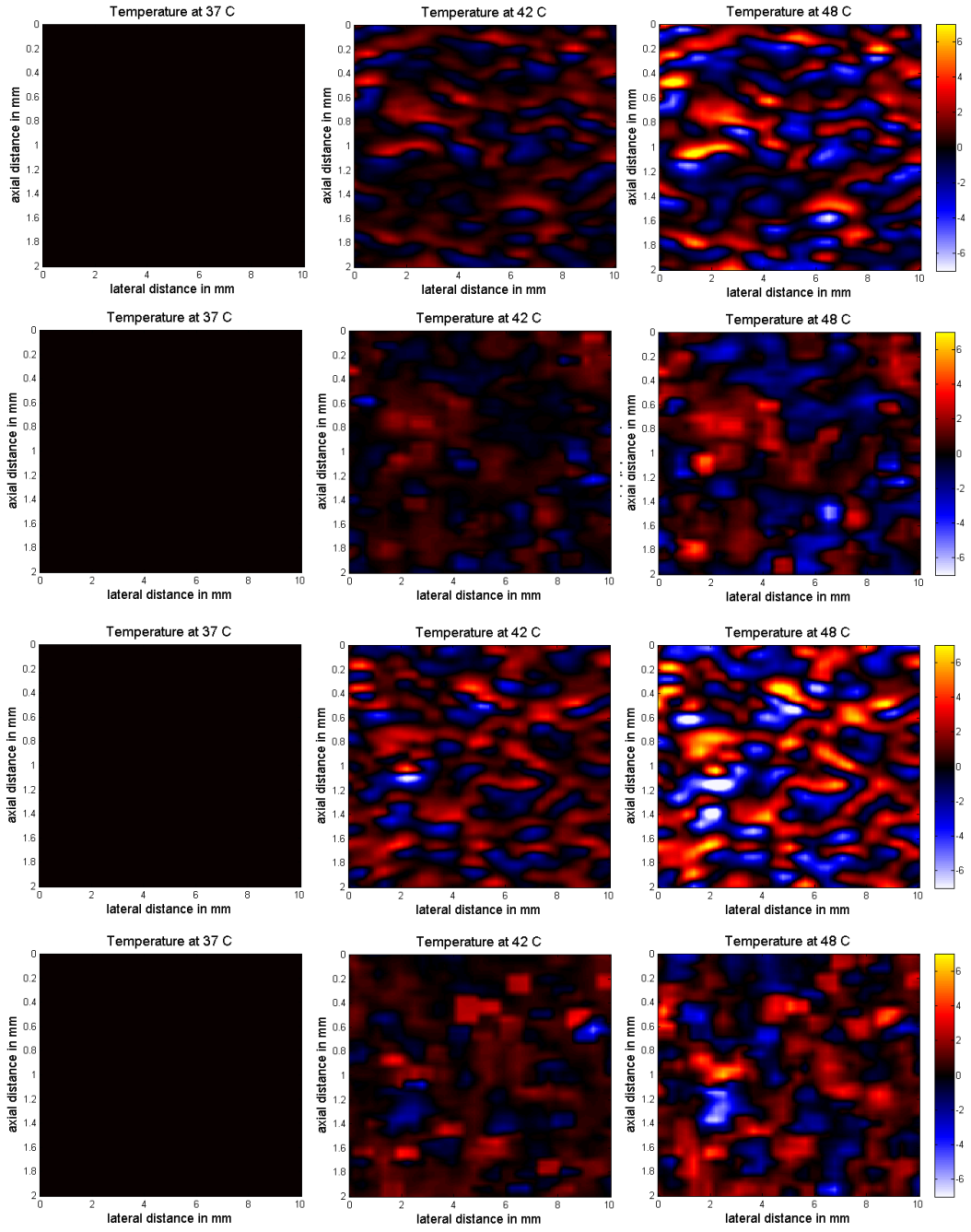

Figure 10. CBE images of Temperature Experiment: First row: Transmitting and receiving with 32 elements with rigid motion tracking method; Second row: Transmitting and receiving with 32 elements with non-rigid motion tracking method; Third row: Transmitting with 64 elements, receiving with 32 elements with rigid motion tracking method; Fourth row: Transmitting with 64 elements, receiving with 32 elements with non-rigid motion tracking method.

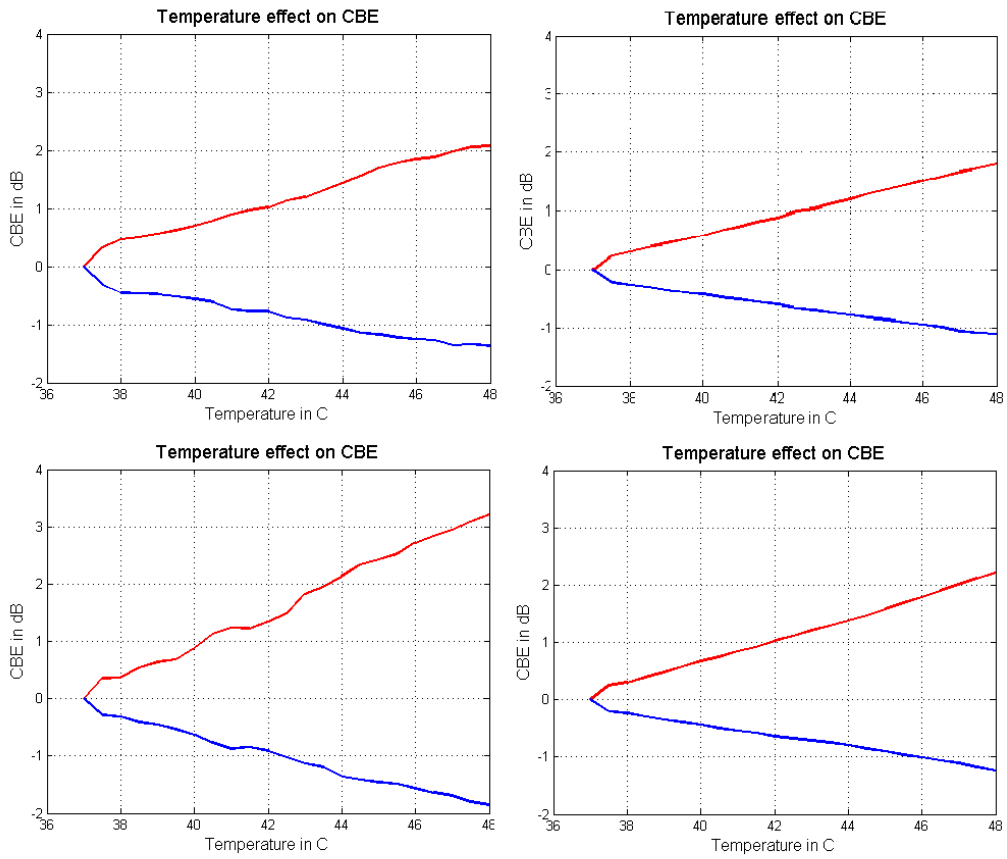

Figure 11. CBE curves of simulation: Upper left: Transmitting and receiving with 32 elements with rigid motion tracking method; Upper right: Transmitting and receiving with 32 elements with non-rigid motion tracking method; Lower left: Transmitting with 64 elements, receiving with 32 elements with rigid motion tracking method; Lower right: Transmitting with 64 elements, receiving with 32 elements with non-rigid motion tracking method. The red line is the positive CBE curve, the blue line is the negative CBE curve.

4.3 Results for elevational displacement experiment

Figure 12 shows the CBE images corresponding to three different elevational

displacement values of the probe. The CBE curves associated with the shifting of the elevational plane are shown in Fig. 13. It can be observed that the CBE curves demonstrated similar behavior to the CBE curves produced in the temperature experiment and simulation. Furthermore, the CBE curves diverged even more for the elevational displacement over 500 μm than for the changes in temperature from 37 to 48 ºC, suggesting a larger effect for the elevational displacements. Note that the shift of 500 μm is less than a half a beamwidth. Since the only changing parameter is the elevational distance, the result suggests that even the small elevational displacement can cause similar CBE as the temperature experiment, which might influence the accurate estimation of temperature. Note that the elevational displacement is hard to get rid of in vivo experiments, due to the respiration and heartbeat.

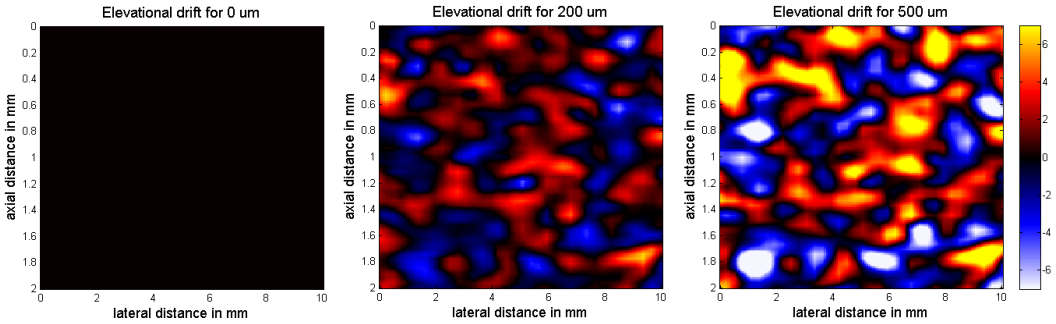

Figure 12. CBE images of elevational displacement experiment. The displacement is 0 um, 200 um and 500 um. The result is quite similar as that of the temperature experiment of Fig. 8. However, even a half beamwidth displacement (500 um) can induce larger CBE than the temperature experiment in Fig.8. This indicates the result is very sensitive to the elevational effect.

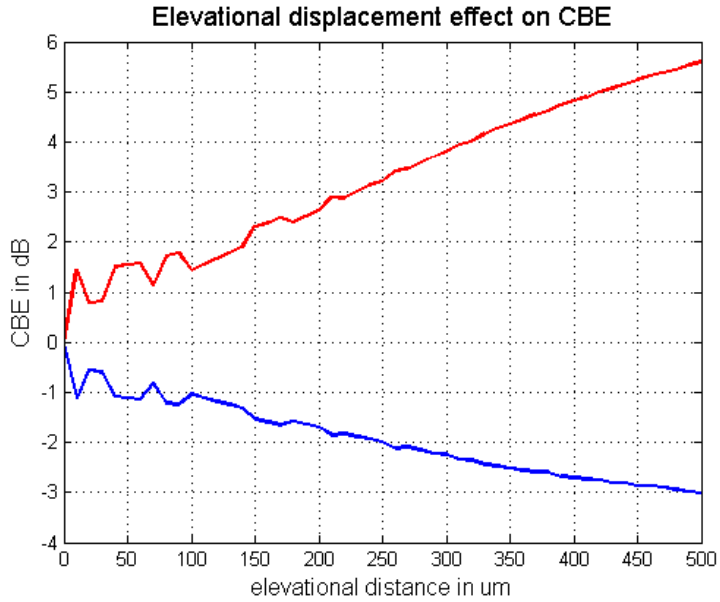

Figure 13. CBE curves of elevational displacement experiment. The red line is the positive CBE curve, the blue line is the negative CBE curve. Again, the CBE curves are similar as those in Fig. 9.

4.4 Results for axial displacement experiment

Figure 14 shows the CBE images constructed by moving the probe away from the phantom. Figure 15 shows CBE curves after shifting the focus a total of 750 um upwards at steps of 10 μm compared to the reference frame. Similar curves were observed for the axial probe motion compared to the results of the simulation and experiments. However, as observed for the axial displacements, the changes in the CBE curves for the focal shifting were larger compared to the temperature experiments. Because the focus depth at -3 dB is 9.6 mm along axial direction, the 0.75 mm is just about 7.8% of the total focus depth. This implies even a small axial displacement can induce a large CBE. Again,

the axial displacement is quite common in experiments with live animals and human.

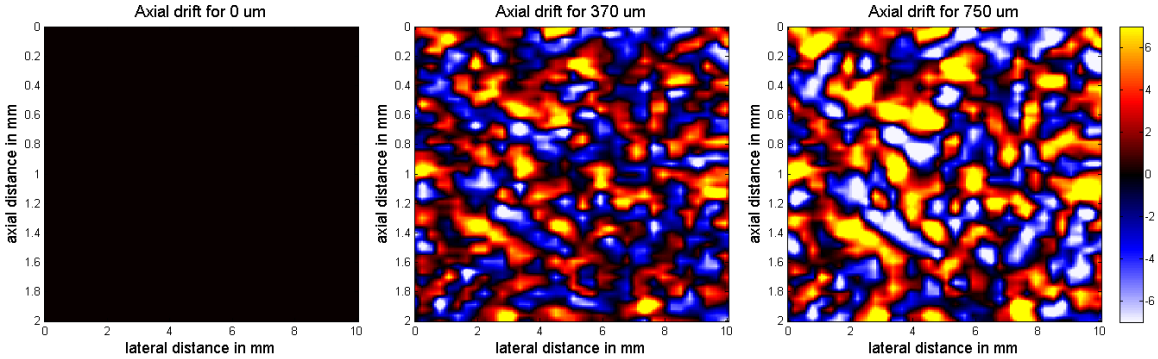

Figure 14. CBE images of axial displacement experiment, the displacement of probe is upward relative to the phantom beneath it, the displacement is 0 um, 370 um and 750 um. As the axial displacement increases, the CBE becoming larger.

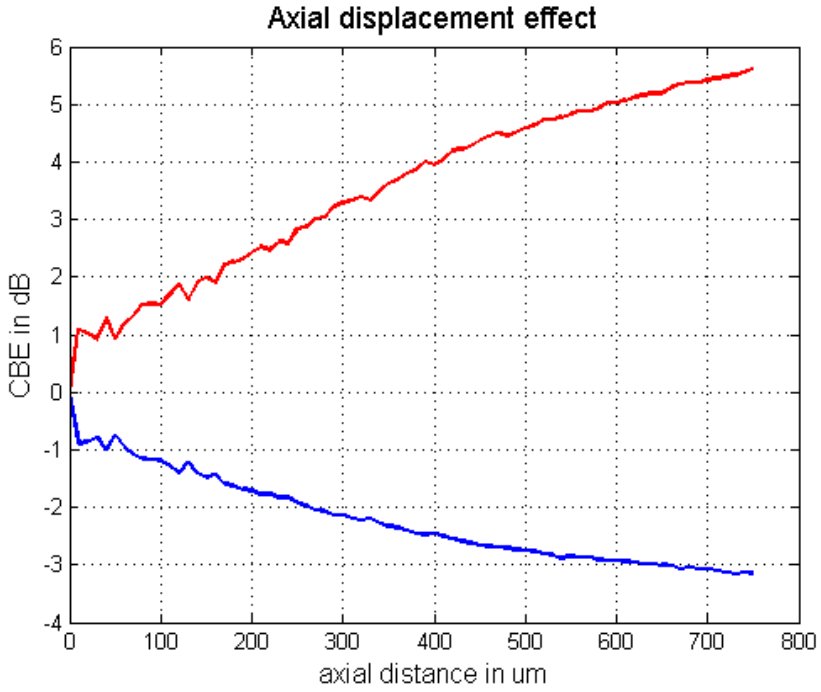

Figure 15. CBE curve of axial displacement experiment. The red line is the positive CBE curve, the blue line is the negative CBE curve. The focus depth at -3 dB is 9.6 mm.

CHAPTER 5 DISCUSSION

5.1 Discussion of simulation results

In the simulations, the only changing parameter was the SOS. The SOS increased from 1520 m/s to 1538 m/s, which corresponds to a rise of temperature from 37 ºC to 48 ºC. Similar CBE images and CBE curves were also observed in [25-28] when increasing the temperature in turkey breast or liver. However, it should be noted that the CBE curve excursions were larger in previous reports [25-28] than what was observed in the simulations, i.e., over the temperature range of 37 ºC to 48 ºC the simulated CBE curves changed by approximately 3 dB in the rigid motion tracking case, whereas those observed in [25-28] changed by up to 6 dB (motion compensated also with rigid tracking method). Therefore, changing the SOS did not entirely account for the CBE curves produced in [25-28]. But this also means that even a change of SOS can lead to such CBE curves without the appearance of lipid and aqueous scatters. Moreover, we can see the impact of different transmitting apertures. If the aperture size is 64 instead of 32, the lateral f number will change from 2.84 to 1.42. The data from Figs. 9 and 11 indicate that a lower f-number yields a larger CBE curve and a more intense CBE image.

Similarly, the rigid motion tracking method will not account for the shrinkage effect, thus causing some error in tracking the same region. Therefore, rigid motion registration will lead to a larger CBE change, as observed in Figs. 9 and

11. However, because the simulation was only simulating point instead of spherical scatterers inside water, not agar, this might cause some disagreement between the experiment data and simulation.

5.2 Discussion of experiment results

A. Temperature experiment

In the temperature experiments, the agar phantoms with glass beads were analyzed. From Figs. 8 and 9, it can be observed that experimental results were similar to the simulation results.

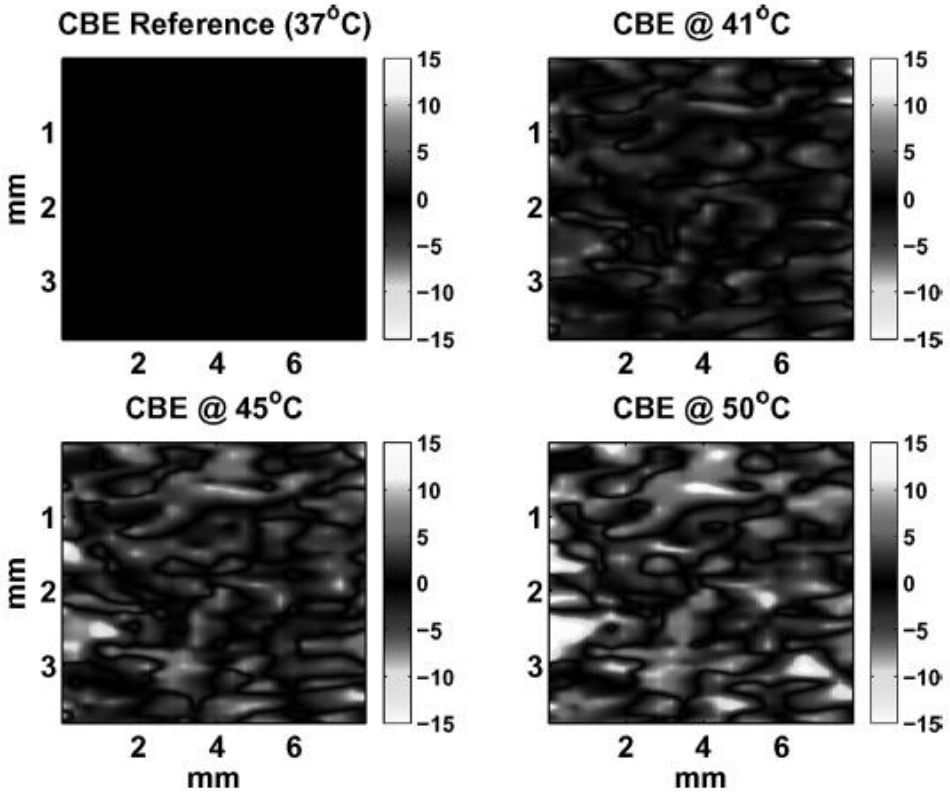

Figure 16. CBE images bovine liver from 37 to 50 ◦ C after compensation for apparent motion. [28],

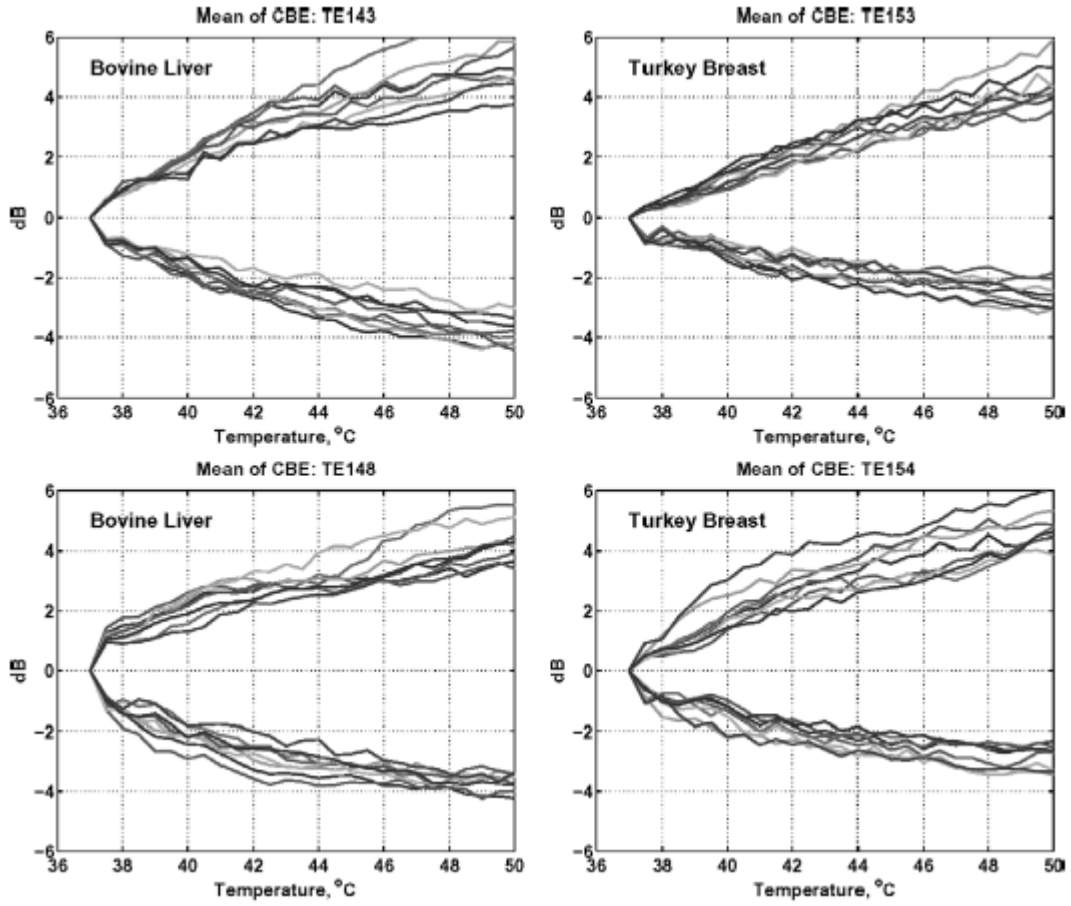

Figure 17. CBE curves for the positive and negative excursions in eight different regions of interest for each of two samples of bovine liver, two samples of turkey breast, and one of pork muscle. [28], Copyright © 2005 IEEE.

A lower f-number led to slightly larger CBE change and using the rigid motion tracking method also yielded larger CBE curves. However, because the phantom was made of agar and glass beads, which is different from the simulation whose scatterers are point scatterers with the same concentration, the result may have some differences. Furthermore, other effects such as deformation and expansion of phantom could not be included in the simulation

and might account for some of the differences between simulation and temperature experiment results.

The scattering effects of glass beads with temperature change is not yet clear, however, the density of glass will not change appreciably with temperature change of 11 ºC. The volumetric thermal coefficient of expansion for glass is β = 27x10-6 1/°C. Therefore, the diameter of the glass beads is expected to increase by 0.03% over a temperature elevation of 11 °C. The changes in SOS and density of the glass beads should be negligible for a temperature elevation from 37 °C to 48 °C. Nevertheless, even if the scattering properties of glass beads changed with temperature, it would only increase or decrease and not do both leading to both positive and negative CBE curves. Therefore, these changes support the hypothesis that CBE can be due to the changing speckle pattern produced by local changes in coherence providing either more local constructive or more destructive interference.

B. Elevational displacement experiment

As Figs. 12 and 13 indicate, the elevational displacement produced similar CBE curves to the temperature effect, but with even larger CBE curves. The elevational image frame shifts produced increasingly larger changes in the speckle pattern which resulted in local changes in the backscattered energy similar to what can be observed with temperature elevations. Even for small

elevational displacements, the CBE curves were observed to diverge rapidly. The -3dB elevational beamwidth is 1.1 mm at 1.6 cm depth (the elevational focus is set 1.6 cm depth for L14-5/38 probe). The total extent of the elevational shift was 0.5 mm, which corresponded to about 45% of the beamwidth at the focus depth. Therefore, even small elevational shifts led to significant CBE change. This leads to the conclusion that using CBE curves to monitor temperature elevations may not be ideal because any out of plane motion can also produce similar CBE curves resulting in incorrect estimates of temperature increase even if registered. Furthermore, expansion of scatterers and tissue in the elevational plane during temperature elevation may also lead to a changing speckle pattern to which CBE appears to be very sensitive. CBE changes from elevational shifts may mislead because it is not known how much elevational displacements or temperature elevations are contributing to the observed CBE. Elevational shifting will occur *in vivo* due to probe or tissue motion of living subjects. Therefore, it appears that the CBE technique is not robust against out of the imaging plane tissue motion.

C. Axial displacement experiment

In the axial displacement experiment, the probe was shifted axially towards the transducer by 750 um at step size of 10 um. Similar CBE image and CBE curve were also produced (Figs 14 and 15). The axial displacement is different from elevational displacement. The local spatial impulse response function will

change, thus the speckle pattern will change. As for the elevational displacement, the cause of the CBE was that the scanning plane shifted to a different location resulting in scanning a different group of scatterers which in turn provided a change in the CBE at a particular location in the imaging plane. Similar to what was concluded for the elevational displacements, the results of the axial displacements would suggest that the CBE method is also sensitive to axial motion and not robust against probe or tissue motion in the axial direction.

5.3 Further considerations of mechanisms responsible for CBE

As observed in the previous results, similar CBE curves can be produced in multiple ways. In each case, the CBE curves are associated with a changing speckle pattern. To help elucidate the mechanism further, a very simple experiment is designed to examine how the speckle pattern change leads directly to CBE.

A. Experiment

If we chose a random region in a B-mode image of 30°C in the temperature experiment, as shown in Fig. 18, the blue box is the “original” piece of data, the red box is the “target” piece of data. The goal is to let the original piece of data gradually transform into the target piece of data. In this process, the CBE is calculated with the method introduced above. This procedure provides one example of gradual transformation of the speckle pattern. No motion tracking

method was required because no actual motion occurred during the transformation.

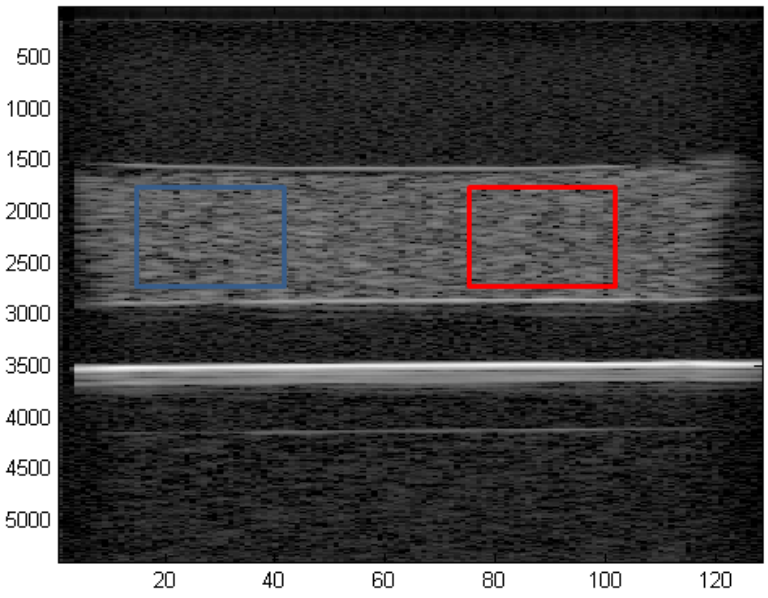

Figure 18. Illustration of two pieces of data chosen to make a gradual change of speckle pattern.

The blue box is the original piece of data, while the red box is the target piece of data

In order to make the gradual transition, interpolation is applied:

$$img_n(i,j) = (img_{original}(i,j) * (N-i) + img_{target}(i,j) * (i-1)) / (N-1). \qquad (5.1)$$

In this case, N=100 was chosen as the number of points between the transformation from the original to the final speckle image. The nth frame is a simple weighted average between the original and target frame. Only the first 13 frames of data are analyzed. With the same data processing method in Chapter II.

B. Results

Figure 19 shows the resultant CBE images of the transformation. Figure 20

shows the resultant CBE curve for the transformation.

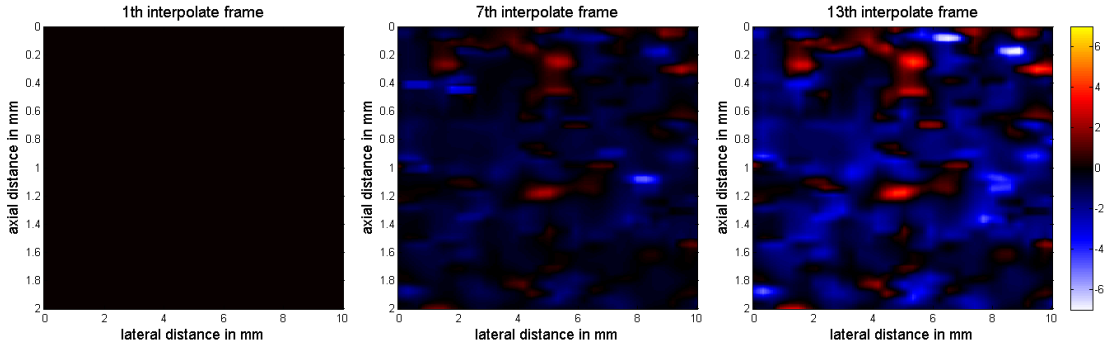

Figure 19. CBE images from gradual transformation experiment.

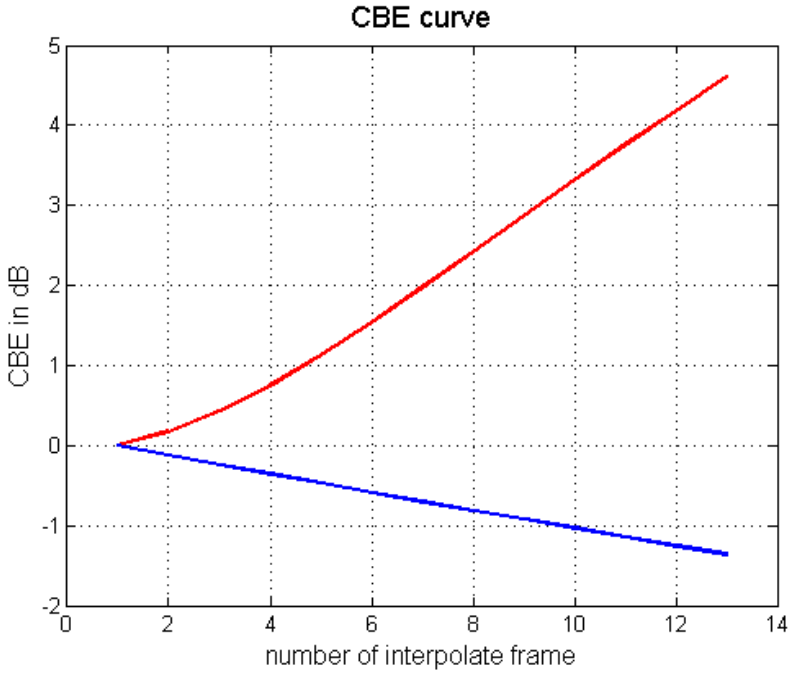

Figure 20. CBE curves from gradual transformation experiment.

C. Discussion

From Figs. 19 and 20, it is observed that even a random change of speckle pattern can produce similar CBE curves. This indicates that the reason for producing the CBE curve and images is a result of changes in the speckle pattern. Therefore, changes in speckle, which can occur from motion, changes

in SOS and even changes in scattering properties, may be present in all cases of practical interest. Separating these effects to correlate to temperature may be difficult in live tissue samples where significant motion is present.

5.4 Further observations regarding CBE curves

Another observation about the CBE curves is that the positive CBE curves typically appear to grow at a larger rate than the negative CBE curves. Part of the explanation of this comes from the nature of the signal changes due to speckle changes. Signal regions with higher reflection signal energy tend to fall after the speckle change, while the regions with lower reflection signal energy tend to rise. Even if the magnitude of signal change is the same, according to equation (1), the CBE of positive change tends to be larger than the CBE of negative change because the reference energy $env_{37^oC}{}^2(i, j)$ for the pixel with positive CBE is smaller leading to a larger dB change.

To further elucidate this mechanism, the experimental data derived from temperature elevations using the 64 element transmit sequence and rigid motion tracking method can be examined. The magnitude of reflection energy (signal square) change and the positive and negative region's averaged background (reference) energy is shown in Fig. 21.

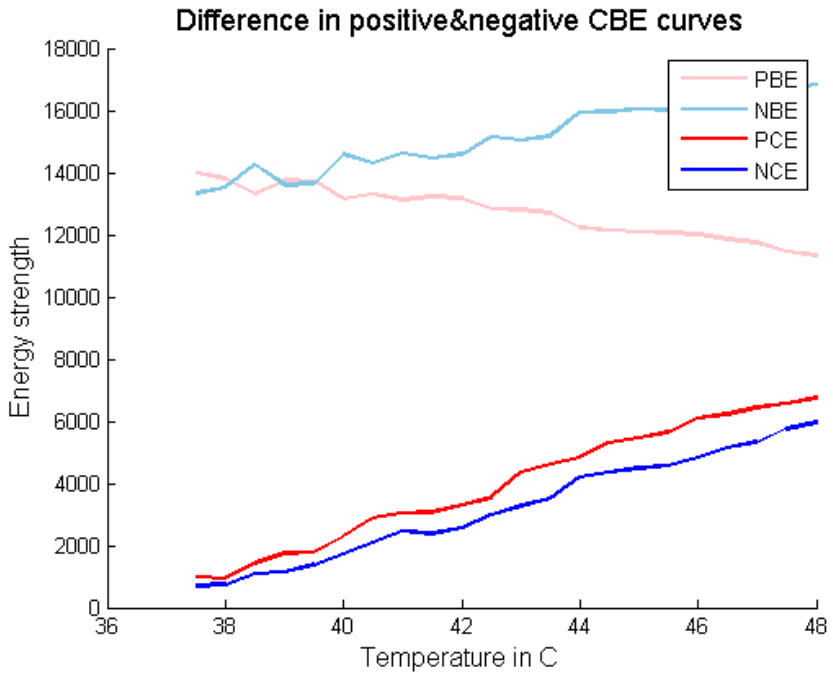

Figure 21. Temperature experiment: Illustration of positive background energy (PBE, pink line); Negative background energy (NBE, light blue line); Positive change of energy (PCE, red line); Negative change of energy (NCE, blue line).

The red line is positive change of energy (PCE):

$$PCE(T) = \underset{i,j}{average}\{env_T{}^2(i,j) - env_{37^oC}{}^2(i,j) > 0\}. \quad (5.2)$$

Where the (i, j) are the indexes of pixels within the data block analyzed. PCE means an average among all the (i, j) for $env_T{}^2(i,j) - env_{37^oC}{}^2(i,j)$, where the term of $env_T{}^2(i,j) - env_{37^oC}{}^2(i,j)$ is greater than zero. The blue line is negative change of energy (NCE):

$$NCE(T) = \underset{i,j}{average}\{env_{37^oC}{}^2(i,j) - env_T{}^2(i,j) > 0\}. \quad (5.3)$$

The pink line is positive background energy (PBE):

$$PBE(T) = \underset{i,j}{average}\{env_{37^oC}{}^2(i,j) : env_T{}^2(i,j) - env_{37^oC}{}^2(i,j) > 0\}. \quad (5.4)$$

The light blue line is negative background energy (NBE):

$$NBE(T) = \underset{i,j}{average}\{env_{37^oC}{}^2(i,j) : env_T{}^2(i,j) - env_{37^oC}{}^2(i,j) < 0\}. \quad (5.5)$$

As observed in Fig. 21, the PCE is gradually increasing (larger than the NCE), but the PBE is gradually decreasing (smaller than the NBE). Therefore, the dB change of positive curve is larger than that of the negative curve in the CBE curves.

Similar behaviors occur for both the elevational displacement experiment and the axial displacement experiment, except for the magnitude of PCE and NCE.

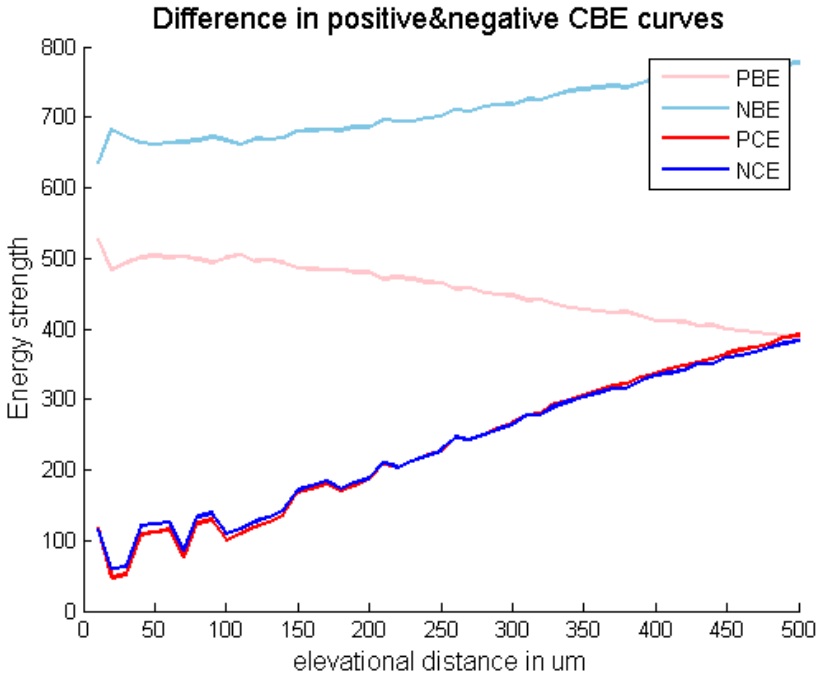

Figure 22. Elevational displacement experiment: PBE, NBE, PCE and NCE.

Figure 22 shows the case of elevational displacement. A small difference can be observed between the case of temperature experiment and elevational displacement experiment. In the temperature experiment case, the PCE is slightly higher than the NCE, however, the PBE is gradually decreasing while

the NBE is gradually increasing. For the elevational displacement case, the PCE and NCE are almost overlapping with each other. This is the same case for axial displacement experiment (shown in Fig. 23).

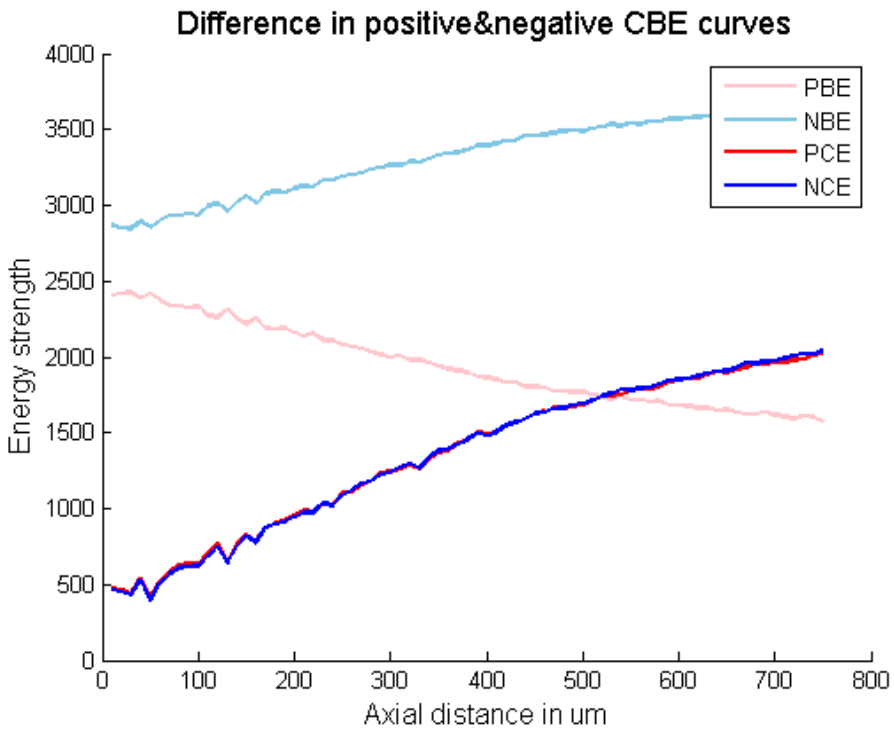

Figure 23. Axial displacement experiment: PBE, NBE, PCE and NCE.

As Fig. 23 shows, the PCE curve is also overlapping with NCE curve. Analysis of CBE curves and their references may provide additional insights into how to distinguish between the CBE effects caused by temperature change and the CBE effects caused by elevational or axial displacement. That is to say, maybe the difference between the PCE and NCE can be used to correlate with temperature instead of the positive and negative CBE curves.

CHAPTER 6 CONCLUSIONS AND FUTURE WORK

6.1 Conclusions

The mechanism of production of CBE was analyzed in theory in [25], the reason of the temperature dependence was assumed to be caused by the different temperature dependence of scatter's density and speed of sound. The scatterers were categorized into two groups, lipid-based scatter and water-based scatter. The lipid-based scatter's scattering cross-section will increase with temperature, the water-based scatter's scattering cross-section will decrease with temperature. However, in the simulation part, the scattering cross-section was set not to change at all, the sole changing parameter is the speed of sound, but we got similar results as shown in Figs. 8&9. In the temperature experiment part, there is only one kind of scatterers-glass beads. If the glass beads' scattering cross-section will change due to temperature, it shall be either increasing or decreasing, however, the result of Fig. 11 shows that both of the increasing and decreasing CBE curves exist, which look similar as the results of [26-28]. These results show that some other factors might also give rise to the CBE, other than the properties of scatterers.

The effects of motion were also analyzed in this work. The motion here is the motion cannot be totally compensated by the motion tracking methods, for example the elevational displacement and axial displacement. The elevational displacement of 500 um (45% of beamwidth), and axial displacement of 750 um (7.8% of the total focus depth) can also split the CBE curves to +5.5 dB and

-3 dB, which might make a significant contribution to the total CBE.

The discussions above indicates that using the CBE curve to estimate the temperature is actually not that robust against motion. And also, the production of CBE is not only due to the properties of scatterers. As the experiment in part 5.3 shows, even a random gradual change of speckle pattern can produce CBE, and similar CBE curves (Fig. 19&20), this result shows that the CBE image and curves are actually a result of random speckle pattern change.

6.2 Future work

Although the simulation and experiment results show that the production of CBE curve is not only caused by the scatter property change, and using the CBE curve to estimate temperature [26-28] is not robust, there are still some problems waiting to be addressed.

Firstly, the fact that only a small displacement in the axial or elevational direction could cause significant CBE changes was unexpected. For example, the -3dB focus depth was about 9.6 mm for the probe used, much larger than the step size (10 um). However, as can be observed in Fig. 15, even for a very small step change, the CBE will change. So understanding why axial and elevational displacements result in such large changes in CBE remains to be understood and future work should examine these mechanisms.

Secondly, the PCE, NCE, PBE and NBE might give more information. In the case where there is only motion, (Figs. 22&23) the PCE and NCE curves

overlapped with each other. However, in the case there is only temperature change (Fig. 21), the PCE curve is larger than the NCE curve. From these results, the difference between the motion caused CBE and temperature caused CBE can be different, these might give rise to the possibility of correlating the difference between the PCE and NCE to temperature to make a more accurate estimate of temperature, which remains to be thoroughly researched in the future.

REFERENCES

[1] M. H. Falk, R. D. Issels, “Hyperthermia in oncology,” Int. J. Hyperthermia, vol. 17, pp. 1 – 18, 2001.

[2] E. L. Jones, J. R. Oleson, L. R. Prosnitz, T.V. Samulski, Z. Vujaskovic, D. Yu, L. L. Sanders, M. W. Dewhirst, “Randomized trial of hyperthermia and radiation for superficial tumors,” J. Clin. Oncol, vol.23, pp.3079 – 3085, 2005.

[3] M. W. Dewhirst, L. Prosnitz, D. Thrall, D. Prescott, S. Cleff,H. C. Charles, J. MacFall, G. Rosner, T. Samulski, E. Gillette, and S. LaRue, “Hyperthermic treatment of malignant diseases: Current status and a view toward the future,” Seminars Oncol, vol. 24, pp. 616 – 625, 1997.

[4] R. J. Myerson, E. Moros, and J. L. Roti Roti, “Hyperthermia,” in Principles and Practice of Radiation Oncology. 3rd ed. C. A. Perez and L. W. Brady, Eds. Philadelphia: Lippincott-Raven, 1998, pp. 637 – 683.

[5] E. Dikomey, H. H. Kampinga, “Review: Hyperthermic radiosensitization: mode of action and clinical relevance,” Int. J. Radiat. Biol, vol. 77, pp. 399-408, 2001.

[6] W. Rao, Z. S. Deng, and J. Liu, “A Review of Hyperthermia Combined With Radiotherapy/Chemotherapy on Malignant Tumors,” Crit. Rev. Biomed. Eng, vol. 38, pp. 101-116, 2010.

[7] Z. Sun and H. Ying, “A multi-gate time-of-flight technique for estimation oftemperature distribution in heated tissue: Theory and computer simulation,”

Ultrasonics, vol. 37, pp. 107–122, 1999.

[8] B. G. Fallone, P. R. Moran, E. B. Podgorsak, “Non-invasive thermometry with a clinical X-ray CT scanner,” Medical Physics, vol. 9, no. 5, pp. 715-721, 1982.

[9] A. H. Mahnken, P. Bruners, “CT thermometry: will it ever become ready for use?” Int. J. Clin. Pract. vol. 65, pp. 1-2, 2011.

[10] M. Lepetit-Coiffé, B. Quesson, O. Seror, B. D. Senneville, B. L. Bail, C. Moonen, H. Trillaud, “Real time monitoring of radiofrequency ablation based on MR thermometry and thermal dose in the pig liver in vivo,” Eur Radiol, vol. 18, pp. 408 416, 2008.

[11] D. Carter, J. MacFall, S. Clegg, X. Wan, D. Prescott, H. C. Charles, and T. Samulski, “Magnetic resonance thermometry during hyperthermia for human high-grade sarcoma,” Int. J. Radiat. Oncol. Biol. Phys., vol. 40, pp. 815–822, 1998.

[12] Committee on the Mathematics and Physics of Emerging Dynamic Biomedical Imaging, “Mathematics and Physics of Emerging Biomedical Imaging,” pp. 144-145, 1996.

[13] T. Bowen, W. G. Connor, R. L. Nasoni, A. E. Pifer, and R. R. Sholes, “Measurement of the temperature dependence of the velocity of ultrasound in soft tissues,” in Ultrasonic Tissue Characterization II. M. Linzer, Ed. Spec. Publ. 525, 1979, pp. 57–61, Washington, DC: U. S. Government Printing Office: National Bureau of Standards.

[14] B. Rajagopalan, J. R. Greenleaf, P. J. Thomas, S. A. Johnson, and R. C. Bahn, “Variation of acoustic speed with temperature in various excised human tissues studied by ultrasound computerized tomography,” in Ultrasonic Tissue Characterization II. M. Linzer, Ed. Spec. Publ. 525, 1979, pp. 227–233, Washington, DC: U. S. Government Printing Office: National Bureau of Standards.

[15] O. Prakash, M. Fabbri, M. Drocourt, J. M. Escanye, C. Marchal, M. L. Gaulard, and J. Robert, “Hyperthermia induction and its measurement using ultrasound,” in Proc. IEEE Ultrason. Symp., 1980, pp. 1063–1066.

[16] S. A. Johnson, D. A. Christensen, C. C. Johnson, J. F. Greenleaf, and B. Rajagopalan, “Non-intrusive measurement of microwave and ultrasound-induced hyperthermia by acoustic temperature tomography,” in Proc. IEEE Ultrason. Symp., 1977, pp. 977–982.

[17] R. Seip and E. S. Ebbini, “Noninvasive estimation of tissue temperature response to heating fields using diagnostic ultrasound,” IEEE Trans. Biomed. Eng., vol. 42, pp. 828–839, 1995.

[18] C. Simon, P. VanBaren, and E. Ebbini, “Two-dimensional temperature estimation using diagnostic ultrasound,” IEEE Trans. Ultrason., Ferroelect., Freq. Contr., vol. 45, pp. 1088–1099, 1998.

[19] R. Maass-Moreno and C. A. Damianou, “Noninvasive temperature estimation in tissue via ultrasound echo-shifts. Part I. Analytical model,” J. Acoust. Soc. Amer, vol. 100, pp. 2514–2521, 1996.

[20] R. Maass-Moreno, C. A. Damianou, and N. T. Sanghvi, “Noninvasive temperature estimation in tissue via ultrasound echoshifts. Part II. In vitro study,” J. Acoust. Soc. Amer., vol. 100, pp. 2522–2530, 1996.

[21] C. A. Damianou, N. T. Sanghvi, F. J. Fry, and R.Maass-Moreno, “Dependence of ultrasonic attenuation and absorption in dog soft tissues on temperature and thermal dose,” J. Acoust. Soc. Amer., vol. 102, pp. 628–634, 1997.

[22] M. Ribault, J. Chapelon, D. Cathignol, and A. Gelet, “Differential attenuation imaging for the characterization of high intensity focused ultrasound lesions,” Ultrason. Imag., vol. 20, pp. 160–177, 1998.

[23] T. C. Robinson and P. P. Lele, “An analysis of lesion development in the brain and in plastics by high intensity focused ultrasound at low-megahertz frequencies,” J. Acoust. Soc. Amer., vol. 5, pp. 1333–1351, 1972.

[24] J. C. Bamber and C. R. Hill, “Ultrasonic attenuation and propagation speed in mammalian tissues as a function of temperature,” Ultrasound Med. Biol., vol. 5, pp. 149–157, 1979.

[25] W. L. Straube and R. M. Arthur, “Theoretical estimation of the temperature dependence of backscattered ultrasonic power for noninvasive thermometry,” Ultrasound Med. Biol., vol. 20, pp. 915–922, 1994.

[26] R. M. Arthur, W. L. Straube, J. D. Starman, E. G. Moros, “Non-invasive temperature estimation based on the energy of backscattered ultrasound,” Med. Phys, vol. 30, pp. 1021–1029, 2003.

[27] R. M. Arthur, W. L. Straube, J. W. Trobaugh, E. G. Moros. “Non-invasive estimation of hyperthermia temperatures with ultrasound,” Int. J. Hyperthermia, vol. 21, pp. 589–600, 2005.

[28] R. M. Arthur, J. W. Trobaugh, W. L. Straube, E. G. Moros, “Temperature Dependence of Ultrasonic Backscattered Energy in Motion-Compensated Images,” ieee trans. ultrason. ferroelect. freq. contr, vol. 52, no. 10, October 2005.

[29] A. Goshtasby, “Image registration by local approximation methods,” Image Vision Comput., vol. 6, pp. 255–261, 1988.

[30] G. E. Christensen, S. C. Joshi, and M. I. Miller, “Volumetric transformations of brain anatomy,” IEEE Trans. Med. Imag., vol. 16, pp. 864–877, 1999.

[31] M. A. Lubinski, S. Y. Emelianov, and M. O’Donnell, “Speckle tracking methods for ultrasonic elasticity imaging using shorttime correlation,” IEEE Trans. Ultrason., Ferroelect., Freq. Contr., vol. 46, pp. 82–96, 1999.

[32] J. M. Fitzpatrick, D. L. G. Hill, and C. R. Maurer, “Image registration,” in Handbook of Medical Imaging. Bellingham, WA: Int. Soc. Optical Eng., vol. 2, ser. Medical Image Processing and Analysis, 2000, pp. 447–513.

[33] F. V. Viola and W. F.Walker, “A comparison of the performance of time-delay estimators in medical ultrasound,” IEEE Trans. Ultrason., Ferroelect., Freq. Contr., vol. 50, pp. 392–401, 2003.

[34] N. R. Miller, J. C. Bamber, and P. M. Meaney, “Fundamental limitations of

noninvasive temperature imaging by means of ultrasound echo strain estimation,” Ultrasound Med. Biol., vol. 28, no. 10, pp. 1319–1333, 2002.

[35] F. L. Lizzi, R. Muratore, C. X. Deng, J. A. Ketterling, S. K. Alam, S. Mikaelian, and A. Kalisz, “Radiation-force technique to monitor lesions during ultrasonic therapy,” Ultrasound Med.

Biol., vol. 29, no. 11, pp. 1593–1605, 2003.

[36] W. Liu, U. Techavipoo, T. Varghese, J. A. Zagzebski, Q. Chen, and F. T. Lee, Jr., “Elastographic versus x-ray CT imaging of radio frequency ablation coagulations: An in vitro study,” Med.

Phys., vol. 31, no. 6, pp. 1322–1332, 2004.

[37] N. R. Miller, J. C. Bamber, and G. R. Ter Haar, “Imaging of temperature-induced echo strain: Preliminary in vitro study to assess feasibility for guiding focused ultrasound surgery,” Ultrasound Med. Biol., vol. 30, no. 3, pp. 345–356, 2004.

[38] J.A. Jensen. “Field: A program for simulating ultrasound systems,” med biol eng comp, vol.34, pp. 351-353, 1996.

[39] J.A. Jensen and N. B. Svendsen. “Calculation of pressure fields from arbitrarily shaped, apodized, and excited ultrasound transducers,” ieee trans ultrason ferroelec freq contr, vol. 39, pp. 262-267, 1992.

[40] R. L. Nasoni, T. Bowen, W. G. Connor, and R. R. Sholes. “In vivo temperature dependence of ultrasound speed in tissue and its application to noninvasive temperature monitoring,” ultrasonic imaging, vol. 1, pp. 34-43,

1979.